coatings

Article

Effect of Carrier Gas on the Gas Sensing Performance of $Co_{1-2x}Ni_xMn_xFe_{2-y}Ce_yO_4$ Double-Substitution Spinel in Flammable Gases and Volatile Organic Compounds

Sunday A. Ogundipe [1,*], Ceboliyazakha L. Ndlangamandla [1], Mmantsae M. Diale [2], Mudalo Jozela [3], Hendrik C. Swart [4], David E. Motaung [4] and Steven S. Nkosi [5,*]

1   Department of Physics, University of Zululand, Private Bag X1001, KwaDlangezwa 3886, South Africa; ndlangamandlac@unizulu.ac.za
2   Department of Physics, University of Pretoria, Private Bag X20, Hatfield 0028, South Africa; mmantsae.diale@up.ac.za
3   National Metrology Institute of South Africa (NMISA), CSIR Campus, Building 5, Meiring Naude Road, Brummeria, Pretoria 0182, South Africa; mjozela@nmisa.co.za
4   Department of Physics, University of the Free State, P.O. Box 339, Bloemfontein 9300, South Africa; swarthc@ufs.ac.za (H.C.S.); david.e.motaung@gmail.com (D.E.M.)
5   Department of Physics, University of Limpopo, Private Bag X1106, Sovenga 0727, South Africa
*   Correspondence: ogundipesunday6@gmail.com (S.A.O.); steven.solethu.nkosi@gmail.com (S.S.N.)

Abstract: The presence of high concentrations of flammable gases and volatile organic compounds in the atmosphere has been widely reported to be detrimental to human survival. A lot of research effort has been put toward finding an efficient means of quick detection of these gases below their 'immediately dangerous to life or health' concentrations. Detecting these gases in an oxygen-deficient environment is a crucial task to consider and has been overlooked. In this research, double-substitution spinel with the chemical formula $Co_{1-2x}Ni_xMn_xFe_{2-y}Ce_yO_4$, where $0 \leq x = y \leq 0.3$, was prepared via the glycol-thermal technique. The final products, following appropriate substitution, were $CoFe_2O_4$ (dried naturally), $CoFe_2O_4$ (dried with infrared lamp), $Co_{0.8}Ni_{0.1}Mn_{0.1}Fe_{1.9}Ce_{0.1}O_4$, $Co_{0.6}Ni_{0.2}Mn_{0.2}Fe_{1.8}Ce_{0.2}O_4$ and $Co_{0.4}Ni_{0.3}Mn_{0.3}Fe_{1.7}Ce_{0.3}O_4$ spinel ferrites. The X-ray diffractometry (XRD), high-resolution transmission electron micrographs (HRTEM) and X-ray photoelectron spectroscopy (XPS) of the samples confirmed the formation of the spinel. The gas sensing performance of these samples was tested at the operating temperature of 225 °C toward liquefied petroleum gas (LPG), ammonia, ethanol and propanol. The $Co_{0.8}Ni_{0.1}Mn_{0.1}Fe_{1.9}Ce_{0.1}O_4$-based sensor was selective to LPG, with a high response of 116.43 toward 6000 ppm of LPG when helium was used as the carrier gas, 3.35 when dry air was the carrier gas, 4.4 when nitrogen was the carrier gas, but it was not sensitive when argon was used as the carrier gas.

Keywords: gas sensor; spinel nanoferrite; oxygen deficiency; carrier gas; LPG sensing

1. Introduction

The ever-growing importance of chemical gas sensing is motivated by the necessity for environmental air quality monitoring, fire hazard prevention, food security and improved clinical diagnosis [1–4]. The expansion of industrialization and urbanization has been accompanied by a tremendous impact on the environment owing to the release of harmful gases and volatile organic compounds (VOCs), posing life-threatening challenges for human survival [5,6]. In addition, explosions of highly flammable and toxic gases, such as liquefied petroleum gas (LPG), H_2S, CO_2 and SO_2, accompanied by the risk of casualty and loss of property, have diverted a lot of attention toward the detection and monitoring of these gases to ensure a safe environment for human existence [7,8]. Gas sensors based on semiconducting metal oxides have been widely investigated for gas detection owing to their ease of fabrication, low production cost, low power consumption

and scalability [1,2,9]. Diverse binary and ternary metal oxides have been explored for gas sensing application. Cobalt-based ferrites, of the widely explored ternary materials, possess interesting characteristics for gas sensing [10]. The cobalt-based ferrite belongs to the spinel group, with the formula AB_2O_4, where A and B are divalent and trivalent metal, respectively. This group of metal oxides are suitable as gas sensors owing to their tolerance for substitution in their structure, oxygen vacancies and adjustable conductivity type [11]. $MgFe_2O_4$ [12], $CoFe_2O_4$ [13], $NiFe_2O_4$ [14], $ZnFe_2O_4$ [15], $CuFe_2O_4$ [16] and $NiCo_2O_4$ [17], among other spinels, have attracted substantial attention in the gas sensing field.

The greatest concern in gas sensing research is the improvement of the sensitivity and selectivity of sensor materials to a target gas. One effective method of achieving this is by introducing a moderate amount of dopant to the structure of a host material [11], causing a change in the electrical properties of the material. Studies reveal that researchers have leveraged this characteristic tunability of the spinel to enhance its sensing performance [11,18]. The cobalt ferrite ($CoFe_2O_4$) has an inverse cubic spinel structure, whose tetrahedral A site is occupied by half of Fe^{3+} ions, and the octahedral B site is occupied by the remaining half of Fe^{3+} and all Co^{2+} ions. Many of the previous works have reported the altered sensing performance of the spinel upon substitution into site A or B of the structure. This study considers a cobalt ferrite material with both A and B site cations partly replaced with Ni and Mn divalent metal cations (on the A site) and Ce trivalent cations (on the B site). It is worth mentioning that the double substitution of the spinel is normal and has been reported previously elsewhere [19]. However, the gas sensing performance of this new class of spinels has never been reported. The understanding is that atmospheric oxygen is chemisorbed on the surface of the sensor when dry air is used as a carrier gas, whereas when an inert gas, such as helium, argon or nitrogen, is used as a carrier gas, an oxygen-deficient ambience is created, resulting in the chemisorption of fewer atmospheric oxygen species on the surface of the sensor. In an oxygen-deficient ambience, we expect the sensor to perform poorly as compared to a normal situation, where atmospheric oxygen is abundant (i.e., in dry air). This conclusion arises from the long-held notion of the active participation of atmospheric oxygen in the gas sensing mechanism of electrochemical gas sensors, as real-time gas sensing takes place in the atmosphere, where there is an abundance of oxygen.

Electrochemical gas sensors operate on the principle of chemoresistivity, i.e., a change in the electrical conductivity or resistivity of thin films upon exposure to the analyte gas. At some specific temperatures, atmospheric oxygen is adsorbed on the sensing surface of an electrochemical sensor, captures the electrons in the conduction band and changes the resistance of the sensor. Upon the exposure of a sensor to an analyte gas, the gas molecules interact with the sensing surface and act as either electron donors or acceptors [20,21]. A reducing gas reacts with chemisorbed oxygen species and causes the release of captured electrons. The release of the electrons into the conduction band results in the increased conductivity of an n-type sensor. If the analyte gas is an oxidizing type, its reaction with an n-type sensor will lead to increased resistivity, as more electrons in the conduction band will be captured by further adsorption of oxygen onto the sensor surface. Generally, gas sensing is believed to be largely caused by oxygen adsorption and desorption on the surface of the metal oxide semiconductor gas sensor [1–21] and, by implication, seems to take place favorably in the presence of oxygen. In addition, the real-life detection of gases occurs in air, where atmospheric oxygen acts as a medium to dilute and carry these gases. This may suggest that chemical gas sensing will only take place or be more supported in an environment with abundant oxygen than in an oxygen-deficient environment, such as in the outer deep space or the lunar south pole, where the lack of atmospheric oxygen is common [22].

NASA had found that metal-oxide-based sensors are suitable for deep space exploration [22]. The drawback would be the low temperatures and insufficient atmospheric oxygen in deep space. In this work, we investigated the chemical gas sensing performance of $Co_{1-2x}Ni_xMn_xFe_{2-y}Ce_yO_4$ in an oxygen-abundant atmosphere and an oxygen-deficient

atmosphere in order to re-create the outer and deep space situations. These carrier gases—dry air, nitrogen, argon and helium—were used to carry the analyte gas and to dilute it into different concentrations. The idea to challenge the widely accepted chemical gas sensing mechanism is novel. The $Co_{1-2x}Ni_xMn_xFe_{2-y}Ce_yO_4$-based sensor exhibited high sensitivity and selectivity toward LPG using helium as the carrier gas when x = y = 0.1. However, the sensitivity and selectivity shifted toward NH_3 gas using dry air as the carrier gas when x = y = 0. When nitrogen was used as the carrier gas, sensitivity and selectivity toward propanol were at x = y = 0.3. The sensors' performance when argon was used as the carrier gas was generally poor toward the tested gases. All these gas sensing measurements were conducted at 225 °C optimal operating temperature. The idea of testing our sensors' performance in different ambient environments, as well as the application of double-substitution $CoFe_2O_4$ spinel nanoferrites in a gas sensing experiment, are unprecedented.

2. Experimental Details

2.1. Synthesis Procedure

$Co_{1-2x}Ni_xMn_xFe_{2-y}Ce_yO_4$, where x = y = 0.0, 0.1, 0.2 and 0.3, were prepared via the glycol-thermal technique. Stoichiometric amounts of $NiCl_2 \cdot 6H_2O$ (98%), $FeCl_3 \cdot 6H_2O$ (98%), $MnCl_2 \cdot 4H_2O$ (99%), $CoCl_2 \cdot 6H_2O$ (97%) and $CeCl_3 \cdot 7H_2O$ (99.9%) obtained were dissolved in 100 mL of distilled water. The ammonium hydroxide solution was added dropwise and mixed under vigorous stirring using a magnetic stirrer for 1 h to adjust the pH to 10. Deionized water was used several times to wash the resulting precipitate until it was free of chloride ions. The precipitate was then added to 300 mL of ethylene glycol for reaction in a PARR 4843 Watlow series stirred pressure reactor at 200 °C for 6 h. The reaction pressures were between 50 and 100 psi, and the stirring speed was 300 rpm. After cooling, the glycol-reacted precipitate was washed using deionized water and heated rapidly to 200 °C for 4 h in the open air. The substance was finally cooled to obtain the as-prepared samples. Some portion of the sample for which x = y = 0 (i.e., $CoFe_2O_4$) was left to dry overnight under 250 W infrared lamp. The powder samples were then annealed for 3 h at 500 °C to obtain the final product and were labeled S1 (IR-lamp-dried $CoFe_2O_4$), S2 (naturally dried $CoFe_2O_4$), S3 ($Co_{0.8}Ni_{0.1}Mn_{0.1}Fe_{1.9}Ce_{0.1}O_4$), S4 ($Co_{0.6}Ni_{0.2}Mn_{0.2}Fe_{1.8}Ce_{0.2}O_4$) and S5 ($Co_{0.4}Ni_{0.3}Mn_{0.3}Fe_{1.7}Ce_{0.3}O_4$).

2.2. Characterization

The crystal structure of each powder sample was studied using a Bruker D8 Advance X-ray diffractometer equipped with a Cu-Kα (λ = 0.1541 nm) radiation source with a a scan rate of 0.3°/min. Scanning electron microscope (SEM, Carl ZEISS Sigma VP-03-67) was used to capture the images of the particle size and surface morphology of the powder samples. A Micrometrics TRISTAR II (USA) surface area analyzer was used for nitrogen adsorption–desorption study and for Brunauer–Emmett–Teller (BET) surface area study. The pore size, pore volume and surface area were measured using nitrogen at 77 K, and the samples were degassed at 150 °C for 3 h. High-resolution transmission electron microscopy (HR-TEM) images were captured by a JEOL 1400 system. PHI 5000 Scanning ESCA Microprobe was used to examine the chemical state of the samples through the X-ray photoelectron spectroscopy (XPS) analysis using a 100 μm diameter monochromatic Al Kα (1486.6 eV) X-ray beam at a pressure of 9.3×10^{-10} Torr. Ar^+ with 2 kV energy, and 2 μA was used for sputter-etching the samples for 1 min at a sputter rate of 15 nm/min. Surface charging was minimized by using a low-energy Ar^+ ion gun and a low-energy neutralizer electron gun. The low-energy peak of Au 4f7 at 83.96 eV and the high-energy peak of Cu 2p3 at 932.62 eV were used for the binding energy calibration. The linearity retardation was set in order to maintain the difference between these two peaks constant at 848.66 eV. To maintain the Ag3d5 peak at 368.27 ± 0.1 eV, the work function of the analyzer was set to 3.7 eV.

2.3. Sensor Fabrication and Measurements

To fabricate the gas sensors, each powder sample was uniformly distributed in ethanol and sonicated for 2 h, and the solution was dropcasted onto the alumina substrate screen-printed with a gold electrode. The other surface of the substrate was heated to 90 °C to remove the organic solvent from the thin sensing layer. For sensing measurement, each of the sensors was simultaneously placed in an airtight chamber with electrical and gas feeds. The measurements of the target gases (LPG, NH_3, ethanol and propanol) at different ppm concentrations were conducted using a KS026K16 (KENOSISTEC model, Italy) gas testing system. These measurements were first performed at the operating temperatures of 175 °C and 225 °C and a constant applied voltage of 5.0 V across the sensors to determine the optimal operating temperature. The responses of the sensors were very low at the operating temperature of 175 °C as compared to that of 225 °C. The transient current curves of the sensors toward LPG using dry air as the carrier gas are presented in Figure S7 of the Supplementary Materials. Once the optimal operating temperature was determined to be 225 °C, the remaining measurements were conducted at 225 °C. Dry air (79% N_2 and 21% O_2) was used to dilute and carry the gases into the chamber for measurements. For gas sensing measurements in an oxygen-deficient ambience, helium, argon and nitrogen were used as the carrier gases at different times. The gas sensing measurements were conducted in a 0.1% RH dry environment. Keithley 6487/E picoammeter/voltage source meter was used to quantify the change in the sensor resistance of the device. The sensor response, *S*, was calculated using the following formula:

$$S = \frac{I_g - I_a}{I_a} \tag{1}$$

where I_g is the current in the presence of gaseous species, and I_a is the current in the air.

3. Results and Discussion

3.1. X-ray Diffraction, Surface Morphology and Chemical Composition

Figure 1a depicts the X-ray diffraction patterns of the pure $CoFe_2O_4$, dried using infrared (IR) lamp, dried in the oven at 200 °C (naturally dried) and the $Co_{1-2x}Ni_xMn_xFe_{2-y}Ce_yO_4$ ferrite spinels resulting from the substitution of tetrahedral A sites and octahedral B sites of $CoFe_2O_4$ with Ni, Mn and Ce atoms in a linearly increasing molar amount.

The substitution was performed at equal molar amounts of x and y, where $0 \leq x = y \leq 0.3$. These substituted spinel nanoferrites were dried naturally at 200 °C for 4 h and subjected to annealing, as described in the Section 2. The final products of the appropriate substitution were $Co_{0.8}Ni_{0.1}Mn_{0.1}Fe_{1.9}Ce_{0.1}O_4$, $Co_{0.6}Ni_{0.2}Mn_{0.2}Fe_{1.8}Ce_{0.2}O_4$ and $Co_{0.4}Ni_{0.3}Mn_{0.3}Fe_{1.7}Ce_{0.3}O_4$, including the unsubstituted $CoFe_2O_4$ spinel ferrites. The samples were labeled S1 (IR-lamp-dried $CoFe_2O_4$), S2 (naturally dried $CoFe_2O_4$), S3 ($Co_{0.8}Ni_{0.1}Mn_{0.1}Fe_{1.9}Ce_{0.1}O_4$), S4 ($Co_{0.6}Ni_{0.2}Mn_{0.2}Fe_{1.8}Ce_{0.2}O_4$) and S5 ($Co_{0.4}Ni_{0.3}Mn_{0.3}Fe_{1.7}Ce_{0.3}O_4$).

The diffraction patterns of the samples with peaks at 2θ positions can be indexed as follows: 30.18° (220), 35.58° (311), 43.39° (400), 53.82° (422), 57.23° (511) and 62.91° (440). The position of the XRD peaks for the samples matched well with the standard XRD pattern for $CoFe_2O_4$ spinel ferrites with JCPDS card number 96-154-0974, and it was in good agreement with the XRD results previously reported elsewhere [19,23–26]. It is noteworthy to mention that at $x = y \geq 0.2$, additional peaks at 2θ positions 28.63, 33.10 and 47.87° were observed. These peaks correspond, respectively, to (111), (200) and (220) planes of CeO_2 with PDF card number 96-721-7888 [19,27–29]. This indicates the formation of CeO_2 secondary phase in the spinel structure. No other phase attributable to Ni and Mn oxides was observed; this is due to the fact that the ionic radii of Ni^{2+}, Mn^{2+} and Co^{2+} were very close to each other, at 0.083, 0.081 and 0.079 nm, respectively. However, the ionic radius of Ce^{3+} (0.101 nm) was greater than that of Fe^{3+} (0.064 nm). As a result, the secondary phase of cerium dioxides was formed as the Ce content increased in the sample. Mkwae et al. [30] reported the formation of CeO_2 as a secondary phase at a higher Ce dopant content during

the synthesis of $MgCe_xFe_{2-x}O_4$ using the hydrothermal method. Many other researchers have previously observed the CeO_2 secondary phase when Ce^{3+} was substituted in their spinel nanoferrites [19,31–33]. In addition, the crystallinity of the sample with x = y = 0.1 was lower than that of the other samples, as some peaks corresponding to the spinel appeared to be absent or inconspicuous, as observed by their low intensity. Table 1 shows the crystallite sizes of the samples, calculated using the Debye–Scherrer equation [34]. Figure 1b–f shows the scanning electron microscope (SEM) images of the spinel nanoferrite samples. The two $CoFe_2O_4$ samples—infrared-lamp-dried and naturally dried—shown in Figure 1b,c possess similar surface morphology, with predominantly fine particles and few agglomerates. Upon addition of impurities to the spinel structure, the difference in surface morphology becomes noticeable, especially at x = y = 0.1 shown in Figure 1d. This sample contains more agglomerates than fine nanoparticles as compared to the previous two samples without dopants—Ni, Mn and Ce cations. The formation of these closely packed agglomerates could be due to the introduction of the Ni, Mn and Ce dopants into the spinel, which might have led to the complication of the spinel structure. Upon substitution with a 0.1 molar concentration of the dopants, the crystallinity of the spinel decreased, as observed earlier in the X-ray diffraction (XRD) analysis. At x = y = 0.2, the spinel looks like solidified magma sparsely covered with agglomerates (see Figure 1e). This is more crystalline than the sample at x = y = 0.1, as can be observed from the high XRD peak intensities in Figure 1a, with secondary phases corresponding to CeO_2. The sample depicted in Figure 1f has the appearance of tightly bound particles.

Table 1. The crystallite sizes, pore size distributions and BET specific surface areas.

| $Co_{1-2x}Ni_xMn_xFe_{2-y}Ce_yO_4$	D_{311} (nm)	Pore Size (nm)	Specific Surface Area (m^2/g)
x = y = 0, IR-lamp-dried	9.99	11.38	66.99 ± 0.29
x = y = 0, naturally dried	11.30	11.96	62.48 ± 0.25
x = y = 0.1	9.28	12.34	72.82 ± 0.34
x = y = 0.2	12.05	10.52	51.93 ± 0.23
x = y = 0.3	12.30	13.29	60.76 ± 0.22

The pore sizes and pore size distributions were estimated by conducting nitrogen adsorption–desorption measurements on the samples. The samples were generally mesoporous, with pore size p, where 2 nm < p < 50 nm. Figure 2 depicts the nitrogen adsorption–desorption isotherm of the $Co_{0.8}Ni_{0.1}Mn_{0.1}Fe_{1.9}Ce_{0.1}O_4$ double-substitution spinel. It is a type IV isotherm [35], which is characteristic of mesoporous materials. The inset corresponds to the pore size distribution. Figure S1 of the Supplementary Materials file shows the isotherms for samples S1, S2, S4 and S5.

Table 1 presents the crystallite sizes of the samples (calculated from the most prominent peak located at the (311) plane of the spinel), the pore sizes and the specific surface areas. The crystallite sizes are observed to vary with dopant amount, while the pore sizes and specific surface areas do not follow a particular order regarding the change in their values upon dopant addition.

Figure 3a–e shows the high-resolution transmission electron microscope (HRTEM) images of the spinel nanoferrites. These spinels are generally crystalline nanoparticles. This is evident in the clear fringes observed on the HRTEM micrographs. The interplanar *d*-spacing (d_{hkl}) fringes of the crystalline plane (Figure 3a) can be attributed to the most prominent ring indexed (311) in the corresponding selected area electron diffraction (SAED) pattern, and it was calculated as d_{311} = 0.255 nm. This value varies slightly among the samples due to the difference in lattice parameters resulting from site loading. The cubic spinel structure was highly expected to undergo expansion as well as shrinkage within the range of dopant amount (0–0.3). The SAED pattern observed for these nanoferrites shows bright crystalline spotted rings, with the (311) plane exhibiting prominence. The SAED ring corresponding to the CeO_2 can also be observed very close to the most prominent ring

of the (311) peak. This agrees well with the XRD result, and the ring corresponds to the (111) plane of the CeO_2 fluorite structure [36], whose interplanar distance (*d*-spacing) is 0.32 nm. It is noteworthy that the secondary phase of CeO_2 was only formed as the Ce^{3+} content increased in the spinel structure.
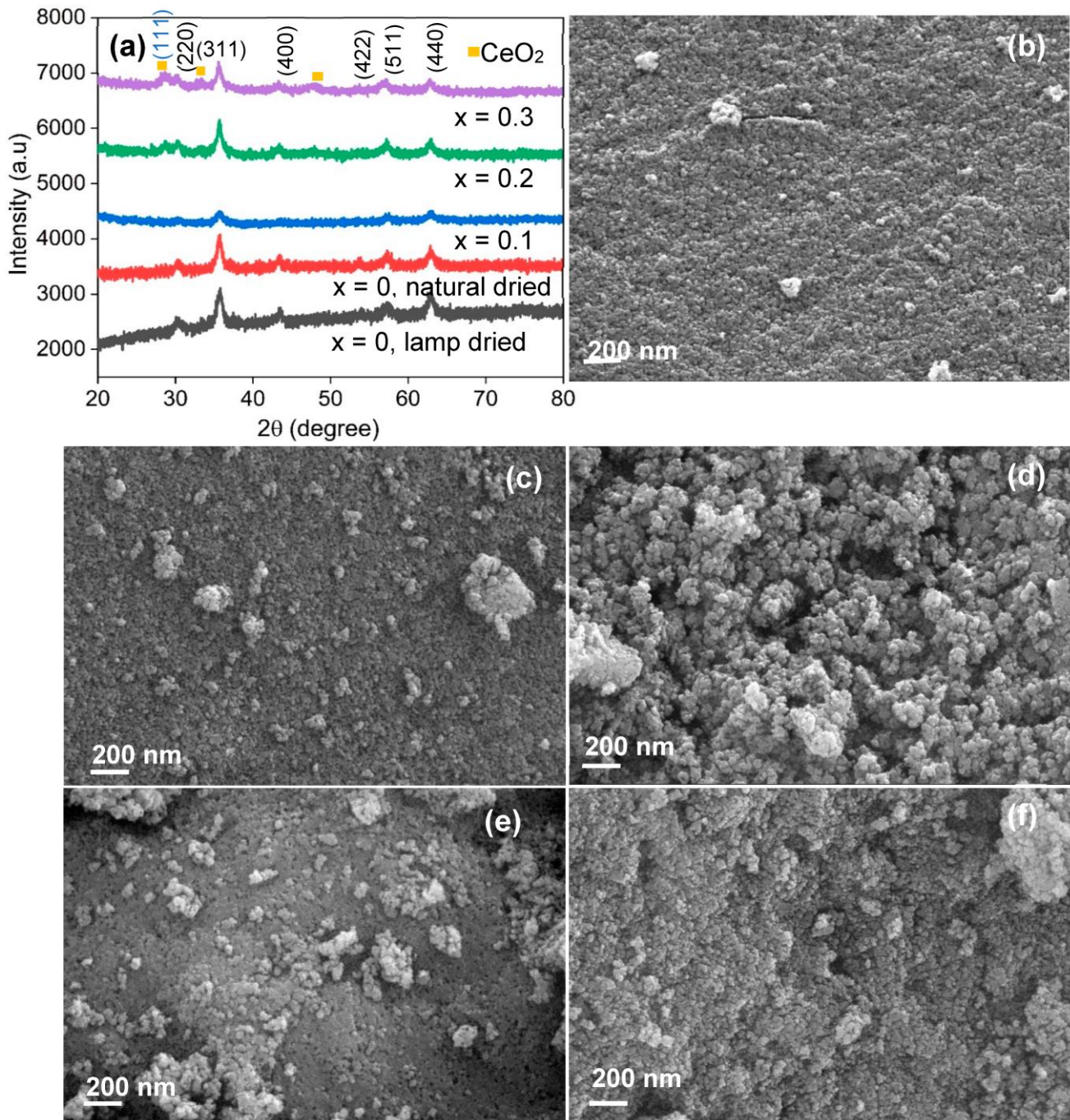
Figure 1. (**a**) The XRD patterns of cobalt ferrite spinel doped with Ni and Mn at tetrahedral A sites, Ce at octahedral B sites. Scanning electron microscopy micrograms of the $Co_{1-2x}Ni_xMn_xFe_{2-y}Ce_yO_4$ samples with (**b**) x = y = 0: dried with infrared lamp, (**c**) x = y = 0: dried naturally, (**d**) x = y = 0.1, (**e**) x = y = 0.2 and (**f**) x = y = 0.3.
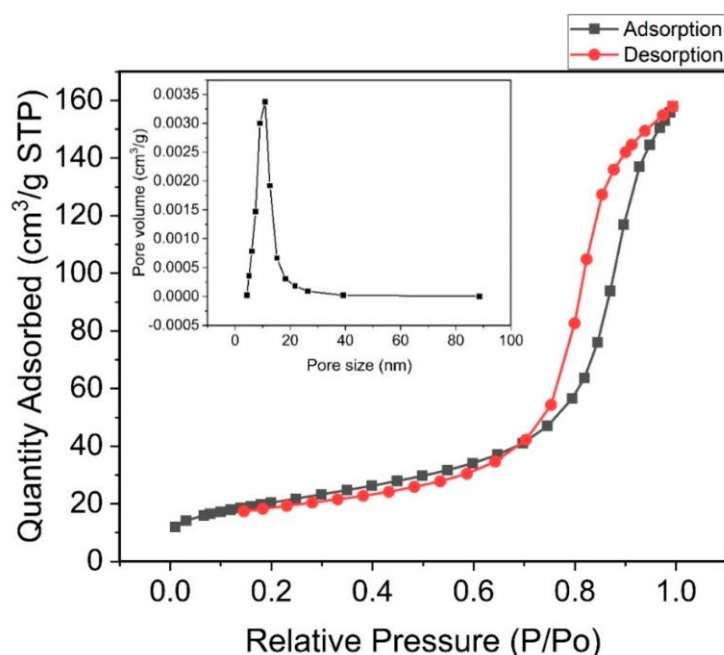
Figure 2. Nitrogen adsorption–desorption isotherms of the $Co_{0.8}Ni_{0.1}Mn_{0.1}Fe_{1.9}Ce_{0.1}O_4$ double-substitution spinel with **Inset:** The corresponding pore size distribution.

Figure 4a–h depicts the X-ray photoelectron spectroscopy (XPS) of the $Co_{1-2x}Ni_xMn_xFe_{2-y}Ce_yO_4$ nanoferrites with $0 \leq x = y \leq 0.3$. The survey spectra shown in Figure 4a,b before and after sputtering the surface with Ar^+ ions were identical, with peaks confirming the presence of Co, Ni, Mn, Fe, Ce, O and C in $Co_{1-2x}Ni_xMn_xFe_{2-y}Ce_yO_4$. The sputtering lasted 1 min at a sputtering rate of 15 nm/min. The similarity of the survey spectra suggests the homogeneity of these nanoferrites. As can be observed in the survey spectra, the Ni 2p peak appears between the edge and the trough of the peak. This may suggest the scarcity or total absence of Ni atoms in the sample composition. Furthermore, the Ni 2p scan (Figure 4d) confirmed the scarcity of Ni atoms, as the peak situated at 848.66 eV and 886.12 eV could not be ascribed to Ni. Figure 4c shows the Co 2p core level spectrum. The fitting peaks at 779.96 eV ascribed to B site Co^{2+} and 781.62 eV ascribed to A site Co^{2+} correspond to Co $2p_{3/2}$ with their satellites at 785.11 eV, while the peak at 796.06 eV corresponds to Co $2p_{1/2}$ with its satellite at 803.25 eV. It is obvious that there are no Co^{3+} cations in the sample, since they normally exhibit peaks centered at 798.5 eV and 783.3 eV while occupying tetrahedral and octahedral sites, respectively [37]. Figure 4e shows the Mn 2p core level spectrum consisting of spin-orbit doublets with their respective satellites.

The Mn $2p_{3/2}$ peaks at 640.68 eV ascribed to Mn^{2+} cations and 642.06 eV ascribed to Mn^{3+} cations apparently have combined satellites located at 645.75 eV. In addition, the peak at 652.96 eV is attributed to Mn $2p_{1/2}$ with its satellite at 657.54 eV. The Ce 3d core level spectrum depicted in Figure 4f exhibits peaks at 882.72 eV and 888.47 eV, which are attributable, respectively, to the Ce^{3+} and Ce^{4+} cations of Ce $3d_{5/2}$. The peak at 901.88 eV is ascribed to Ce $3d_{3/2}$ with its satellite peak at 916.21 eV. The Fe 2p spectrum shown in Figure 4g comprises two spin-orbit doublets situated as follows: Fe 2p3/2 (710.43 eV, Fe^{3+} in B sites and 712.45 eV, Fe^{3+} in A sites) with its combined shake-up satellites at 718.20 eV and Fe $2p_{1/2}$ (724.10 eV, Fe^{3+} in B sites and 725.61 eV, Fe^{3+} in A sites) with its satellites at 732.32 eV. The positions of the binding energy of Co 2p and Fe 2p peaks and their satellites confirm the oxidation state of Co and Fe (Co^{2+} and Fe^{3+}) in the sample. The spectra also indicate the presence of Co and Fe at the octahedral and tetrahedral sites [19]. The O 1s spectrum (Figure 4h) consists of three peaks ascribed to O-Ce (centered at 529.00 eV), O_L of the metal {Fe-O/Co-O/Ni-O} (centered at 529.9 eV) and O_V/O_c (centered at 531.23 eV). O_L is the oxygen inherent in the sample; O_V signifies the oxygen-deficient sites in the sample.

O_C is connected to surface oxygen in the sample. Figures S2–S5 of the Supplementary Materials show the XPS spectra of samples S1, S2, S4 and S5.
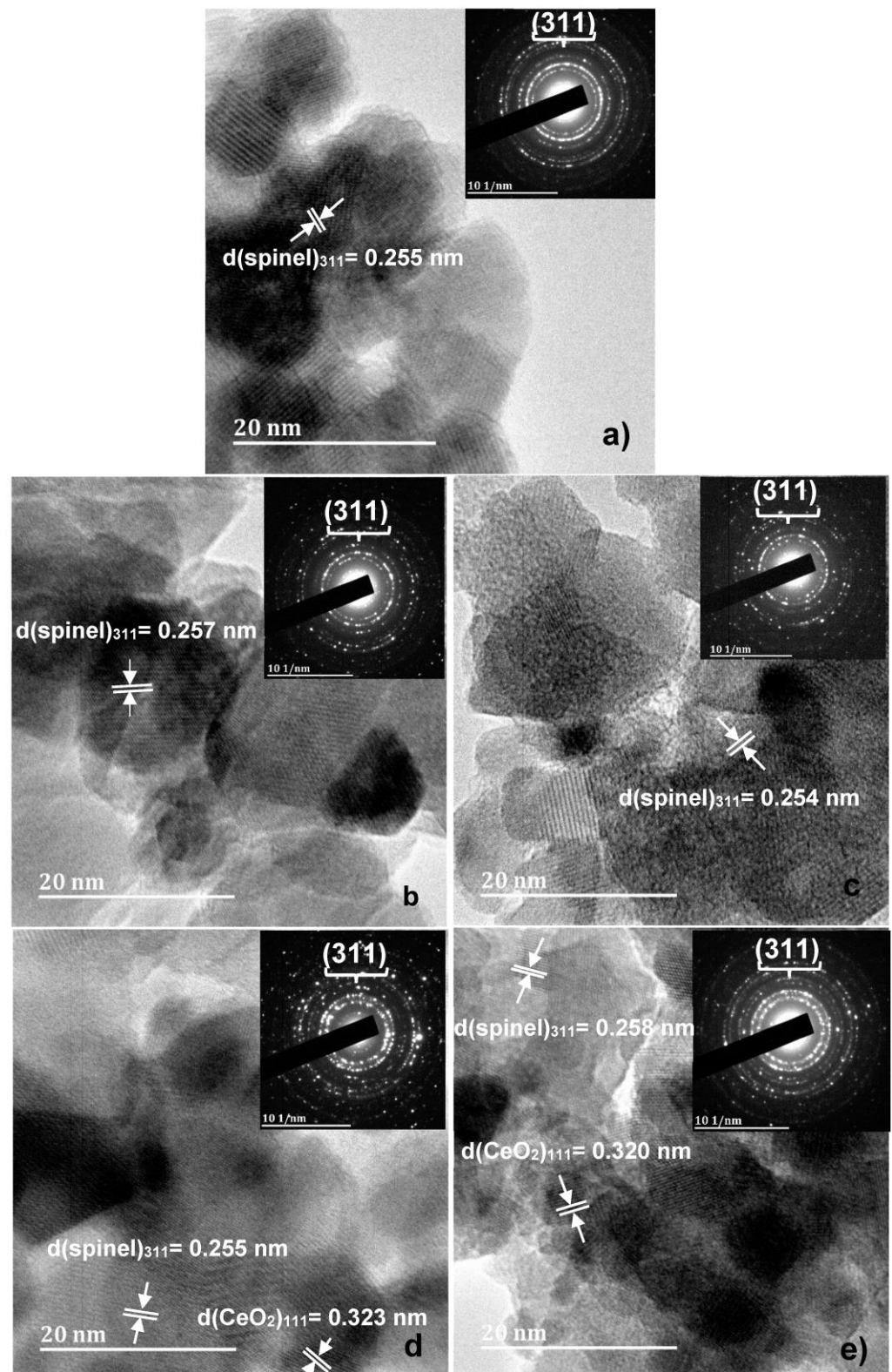
Figure 3. HRTEM images of the $Co_{1-2x}Ni_xMn_xFe_{2-y}Ce_yO_4$ samples with (**a**) x = y = 0: dried with IR lamp, (**b**) x = y = 0: dried naturally, (**c**) x = y = 0.1, (**d**) x = y = 0.2 and (**e**) x = y = 0.3. The insets are the corresponding selected area electron diffraction (SAED) patterns.
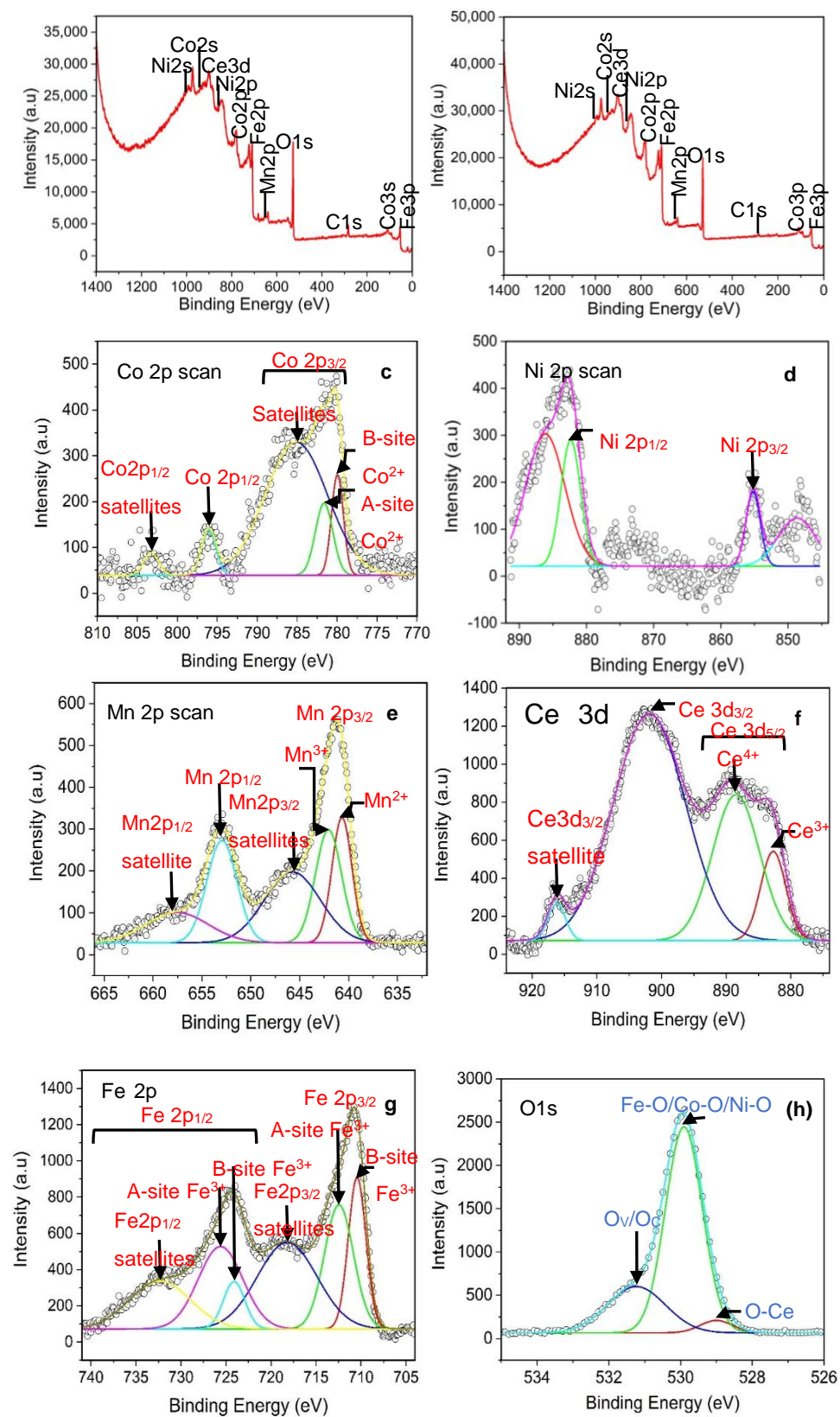
Figure 4. XPS spectra of $Co_{1-2x}Ni_xMn_xFe_{2-y}Ce_yO_4$ sample, for which x = y = 0.1: (**a**) survey spectrum before sputtering, (**b**) survey spectrum after sputtering, (**c**) Co 2p scan, (**d**) Ni 2p scan, (**e**) Mn 2p scan, (**f**) Ce 3d scan, (**g**) Fe 2p scan and (**h**) O 1s scan.

Various deconvolutions of the O 1s peaks are presented in Table 2. Chemisorbed oxygen is only present in two of the samples, while the existence of oxygen vacancy and lattice oxygen is generally observed.

**Table 2.** Deconvolution of O 1s peaks from XPS analysis.

$Co_{1-2x}Ni_xMn_xFe_{2-y}Ce_yO_4$	O_L:	$(O_V + O_C)$:	$(O_L + O_V)$:
x = y = 0, IR-lamp-dried	0.55	0.45	-
x = y = 0, naturally dried	0.69	O_V = 0.31	-
x = y = 0.1	0.04	0.96	-
x = y = 0.2	0.84	O_V = 0.16	-
x = y = 0.3	0.61	O_V = 0.39	-

3.2. Gas Sensing Properties

The sensors were exposed to ethanol, propanol, ammonia and LPG at the operating temperature of 225 °C. The concentration range for each of the target gases was based on the recommended exposure limits. Dry air, helium, nitrogen and argon were used as the carrier gases and for analyte gas dilution to produce different concentrations.

Figure 5 depicts the selectivity plots of $Co_{1-2x}Ni_xMn_xFe_{2-y}Ce_yO_4$, $0 \leq x = y \leq 0.1$, double-substitution spinel (i.e., S3) toward ethanol, propanol, ammonia and LPG using dry air and helium gas as the carrier gases. It should be mentioned that the gas sensing results obtained when nitrogen and argon were used as the carrier gases are not included here, as these did not produce good gas sensing performance as expected. These results are shown in Figure S6 of the Supplementary Materials. Figure 5a shows that when dry air was used as a carrier and to dilute the analytes, sensors S1 and S3 were more sensitive to ethanol vapor. However, propanol vapor could be highly detected by the S1 sensor. Moreover, sensor S3 was highly sensitive to ammonia. Furthermore, LPG could be detected by S1. Overall, sensor S3 gave the highest response of 7.95 to ammonia. The whole situation changed unexpectedly when helium was used as the carrier gas and to dilute the analytes. The expectation was that helium is an inert gas and will create an oxygen-deficient atmosphere inside the sensing chamber, resulting in a decrease in the sensors' sensitivity toward the analyte gas. The opposite is observed in Figure 5b. Sensor S3 was extremely sensitive and selective to LPG at 6000 ppm concentration, with a response of 116. Interestingly, these experiments, which were designed to demonstrate the performance of semiconductor gas sensors in different atmospheres, were accompanied by some anomalies. Figure 5c depicts the transient current plot of the LPG concentrations on the S3 sensor. The results show an increasing response with LPG concentration until 6000 ppm is reached. Thereafter, the response begins to drop with further increase in the concentration. However, toward the 10,000 ppm concentration, the response is slightly higher than that toward the 9000 ppm concentration. This can be attributed to the fact that at 10,000 ppm, the carrier gas is almost unavailable in the chamber. All the maximum gas analyte concentrations should look the same, regardless of the carrier gas. The reason for the decrease in the response after 6000 ppm is not clear and neither is the high response when helium was used as the carrier gas in comparison to the performance when dry air was used.

In Figure 5d, the transient current plot of the sensor toward LPG using dry air as the carrier gas is shown. The sensor exhibits n-type characteristics toward the first three concentration cycles of LPG: 1000, 2000 and 3000 ppm. At the peak corresponding to the 3000 ppm concentration, a large split is observed, which is attributed to fluctuation in the operating temperature, as once observed by Mkwae et al. [30]. However, from 4000 ppm onwards, the charge carrier transition begins to occur in the sensor upon LPG sensing. The response of this sensor toward 3000 ppm of LPG is 3.35.
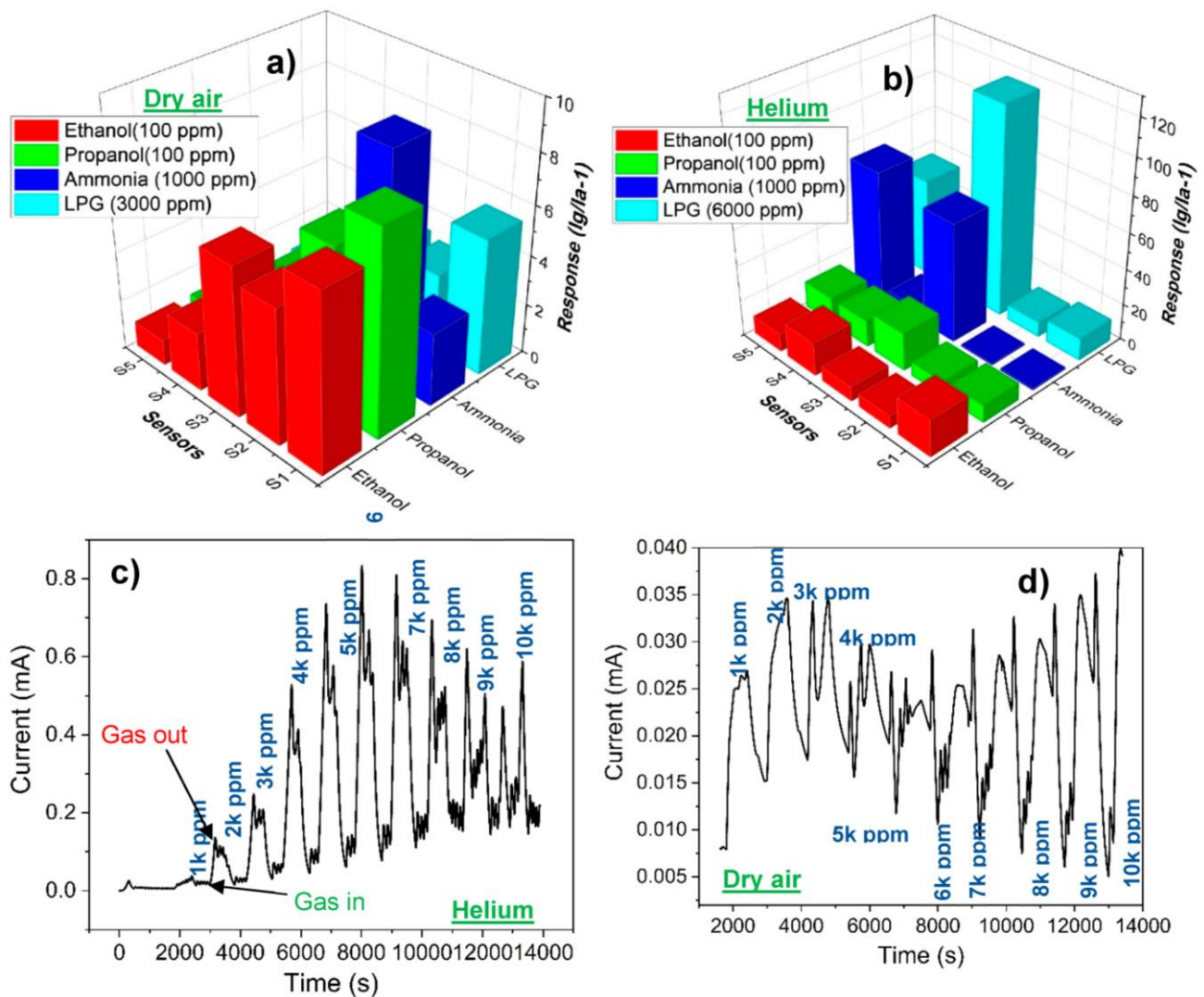
Figure 5. Three-dimensional selectivity plots of $Co_{1-2x}Ni_xMn_xFe_{2-y}Ce_yO_4$ double-substitution spinel toward (**a**) ethanol, propanol, ammonia, and LPG in dry air atmosphere; (**b**) ethanol, propanol, ammonia and LPG (6000 ppm) in helium gas atmosphere; (**c**), transient current plot of S3 toward LPG in helium atmosphere and (**d**) transient current plot of S3 toward LPG in dry air atmosphere.

The LPG sensing of sensor S3 in dry air atmosphere was characterized by two distinct phenomena, namely current oscillation, resulting from fluctuation in the operating temperature, and charge carrier transition, from n- to p-type. The response of this sensor was 5.87 (10,000 ppm). The arrow at the bottom of the curve indicates the moment LPG was allowed into the chamber, while the arrow at the top of the curve indicates the moment LPG was stopped from entering the chamber. In helium gas atmosphere, there was no charge carrier transition observed in the sensors upon LPG detection; rather, there was a decrease in the sensors' response from 7000 ppm concentration of LPG in addition to the observed current oscillation, which occurred at the peak, as well as at the sensors' relaxation. Generally, the sensors behaved abnormally upon LPG detection when helium was used as the carrier gas. The response increased from 1000 ppm to 6000 ppm and then decreased from 7000 ppm to 10,000 ppm. This made the response of S3 at 10,000 ppm (81.73) lower than that at 6000 ppm (116.43). The response could have been much greater than 116.43 had the abnormal decrease in response not occurred. Moreover, while the sensors' response pattern toward other gases was normal, it was generally abnormal toward LPG (and occasionally toward NH_3), irrespective of the carrier gas used.

Figure 6 shows the response patterns of the sensors toward LPG in dry air atmosphere and in helium gas atmosphere. The peaks labeled 1–10 correspond to 1000–10,000 ppm LPG concentration with 10 equal intervals. Figure 6a is the response pattern of the naturally dried $CoFe_2O_4$-based sensor toward LPG in dry air atmosphere. This pattern is like that of the IR-dried sample. The pristine samples did not undergo charge carrier transition; rather, their LPG sensing performance was accompanied by current oscillation, which became prominent with gas concentration. At concentrations of 5000 to 7000 ppm, the frequency of the oscillation was high, while the amplitude was higher from 8000 to 10,000 ppm concentrations, as seen in Figure 6a. This current oscillation was caused by the fluctuating operating temperature during LPG sensing. This anomaly was discussed elsewhere [38]. The response pattern of the sensor (S5), fabricated from the sample with the chemical formula $Co_{0.4}Ni_{0.3}Mn_{0.3}Fe_{1.7}Ce_{0.3}O_4$, is depicted in Figure 6b. This pattern is similar for all the doped samples. They exhibited charge carrier transition (n- to p-type) upon LPG detection. Figure 6c,d show the response patterns of S2 and S5, respectively, toward LPG in helium gas atmosphere. S1 and S2 were fabricated from the pure samples, and they exhibited similar sensitivity patterns, while S3, S4 and S5 were doped samples, and they also exhibited similar sensitivity patterns. When nitrogen was used as the carrier gas, the sensitivity pattern of the sensors toward LPG was similar to the one exhibited when dry air was used. There was a charge carrier transition of the sensors from n- to p-type. Additionally, there were series of current oscillations at the peaks of the response. When argon was the carrier gas, the performance of the sensors was generally poor and unquantifiable. The gas sensing performance of the sensor (S3) toward LPG in dry air, nitrogen gas, helium gas and argon gas is compared in Table 3. The resistance values presented in Table 3 indicate the sensor resistance in the carrier gas before the target gas, i.e., before LPG was introduced into the chamber. The idea of gas sensing using different carrier gases (as carried out in this work) is unprecedented. The outstanding response of the $Co_{0.8}Ni_{0.1}Mn_{0.1}Fe_{1.9}Ce_{0.1}O_4$ sensor (S3) toward LPG in helium gas was noteworthy, and it could be suggested that helium gas created a more conduction-enhancing condition for the sensor than dry air, nitrogen gas and argon gas. It was probably acting as a catalyst in the reaction between the sensing layer and the gas. Moreover, the optimal resistance for best performance appears to be attained in helium gas, as can be observed in Table 3. This could be the reason for higher conductivity in the sensor when the LPG was allowed into the chamber with helium as the carrier gas. The responses presented in Table 3 are toward 3000 ppm of LPG in dry air, 3000 ppm of LPG in helium gas and 3000 ppm of LPG in nitrogen gas. The highest response was recorded when dry air was used as the carrier gas toward ammonia in sensor S2. The response was 9 toward 1000 ppm; the transient current curve of the sensor is shown in Figure 6e.

Table 3. Comparison of gas sensing performance of the sensor (S3) toward LPG (3000 ppm) in various carrier gases.

Carrier Gas	Resistance (kΩ)	Response
Dry air	641.03	3.34
Nitrogen	28.57	4.37
Helium	769.23	73.11
Argon	-	-
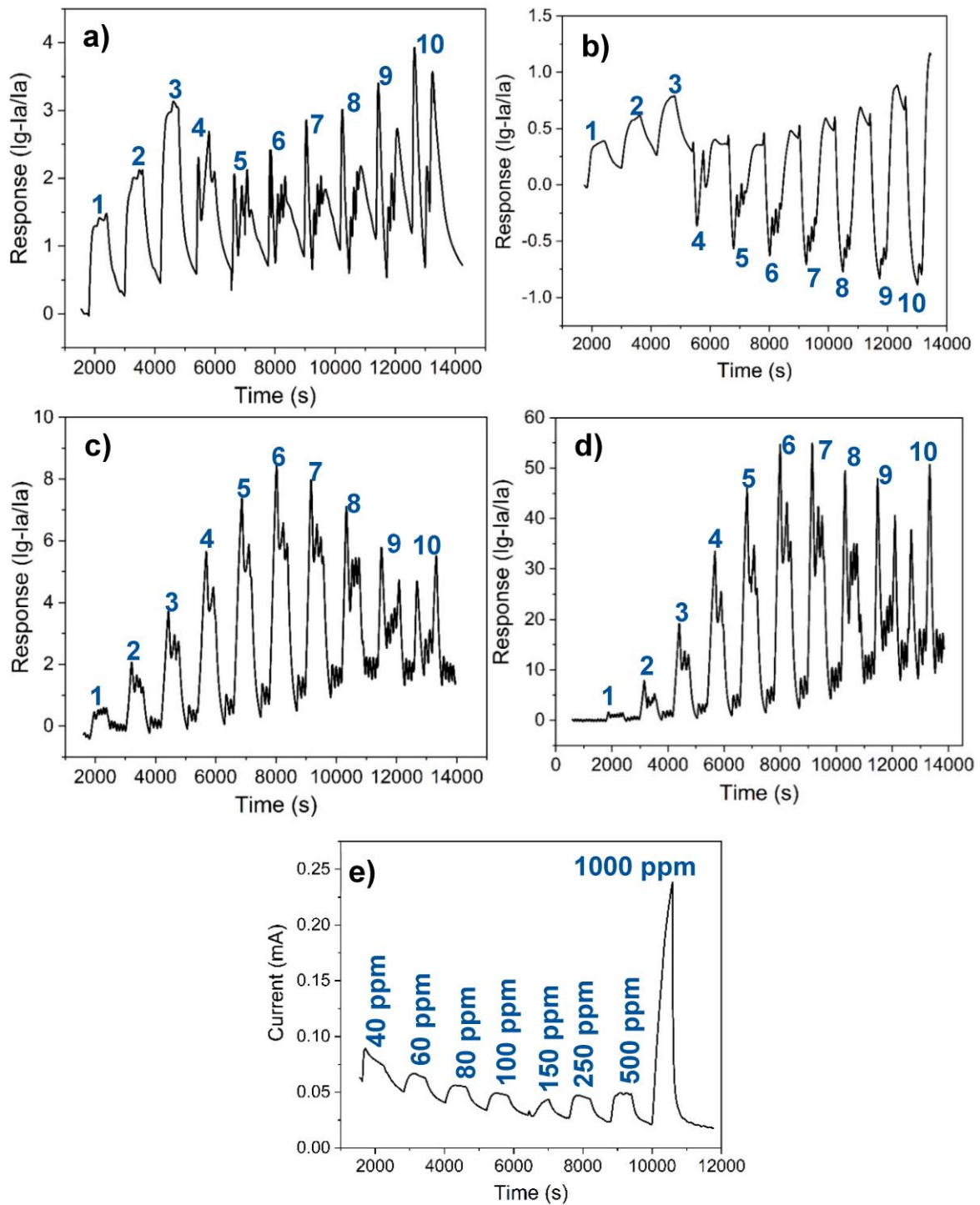
Figure 6. Gas sensing response pattern of (**a**) S2 toward LPG using dry air as carrier gas, (**b**) S5 toward LPG using dry air as carrier gas, (**c**) S2 toward LPG using helium as carrier gas, (**d**) S5 toward LPG using helium as carrier gas and (**e**) transient current curve of S2 toward ammonia gas using dry air as carrier gas.

Gas Sensing Mechanism

Figure 7 illustrates the gas sensing mechanism of the $Co_{0.8}Ni_{0.1}Mn_{0.1}Fe_{1.9}Ce_{0.1}O_4$-based sensor in the different ambient conditions (oxygen-abundant and oxygen-deficient) in which it was operated to determine its gas sensing performance. At an operating temperature of 225 °C, atmospheric oxygen is chemisorbed on the surface of the sensor as O^- oxygen species (Figure 7a), as illustrated in Equations (2)–(5). These oxygen species capture

the free electrons at the conduction band, creating a depletion layer on the sensor [39,40], and thus increase the resistivity of the n-type sensor. When the target gas (LPG, which is a reducing gas) was introduced into the chamber, it reacted with the chemisorbed oxygen on the sensor surface to produce water and carbon dioxide (Figure 7b). The surface reduction in the sensor's sensing layer led to the release of the captured electrons, causing the thinning of the depletion layer and resulting in increased conductivity of the sensor [39–41]. When helium was used as the carrier gas (Figure 7c), the sensor resistance (27.95 kΩ) was observed to be far lower than that observed when air was used (see Table 3). This implies the availability of more electrons at the conduction band of the n-type semiconductor-based sensor as a result of a very thin depletion region. This could be due to the displacement of oxygen from the chamber, where, at the operating temperature, it could have been adsorbed again to the sensor surface and reduced the quantity of electrons or hindered the mobility of electrons in the conduction band. Nevertheless, it could not be explicitly stated that some chemisorbed species of oxygen were no longer available on the sensor's surface. It could rather be suggested that there was a limited amount of them; otherwise, the current would have remained the same when LPG was allowed into the chamber (as adsorption/desorption of oxygen is currently understood to be the principle upon which the operation of electrochemical gas sensors is based) [20,42,43]. The sensor's response was observed to increase with increasing concentration of the target gas (LPG). The effect of helium was more noticeable when it was used as the carrier gas for LPG (depicted in Figure 7d). The relatively high sensor response toward LPG (using helium as the carrier gas) indicates the catalytic effect of helium in the process. While helium did not actually participate in the chemical reaction (being inert, as shown in Figure 7c), it is obvious that it facilitated the reaction of LPG with the residual oxygen species on the sensing layer by easily bringing LPG into close contact with the sensing layer and thus aiding in the further thinning of the depletion layer, as shown in Figure 7d.

$$O_2(\text{gas}) \rightarrow O_2(\text{ads}) \tag{2}$$

$$O_2(\text{ads}) + e^- \rightarrow O_2^-(\text{ads}) \qquad T < 100\ ^\circ C \tag{3}$$

$$O_2^-(\text{ads}) + e^- \rightarrow 2O^-(\text{ads}) \qquad 100\ ^\circ C < T < 300\ ^\circ C \tag{4}$$

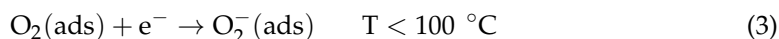$$O^-(\text{ads}) + e^- \rightarrow O^{2-}(\text{ads}) \qquad T > \ ^\circ C \tag{5}$$

Figure 8a shows the transient current curve resulting from the detection of three cycles each of 5000 ppm, 6000 ppm and 7000 ppm LPG concentrations by the sensor (S3). The sensor could not maintain the same response toward three cycles of 5000 ppm concentration of LPG. Its response toward three cycles of 6000 ppm concentration was consistent, while its response to three cycles of 7000 ppm concentration was similar to the one observed for the 5000 ppm concentration but with a lower response. The decrease in the response, which occurred toward 7000 ppm in comparison with the 6000 ppm concentration, was consistent with the result obtained earlier. The test was carried out over 10 months after the initial measurement. The response of the sensor decreased to 12.39 over this period.

Figure 8b shows the sensitivity plot of the sensor (S3) toward 5000 ppm and 6000 ppm of LPG using helium as the carrier gas in the presence of 50% relative humidity. The response of the sensor under this condition was 10.98 as compared to 12.39 under helium gas ambient condition (with 0.2% relative humidity). The sensor was not much affected by the high humidity; this indicates its potential for LPG detection and monitoring in an atmosphere with high relative humidity.
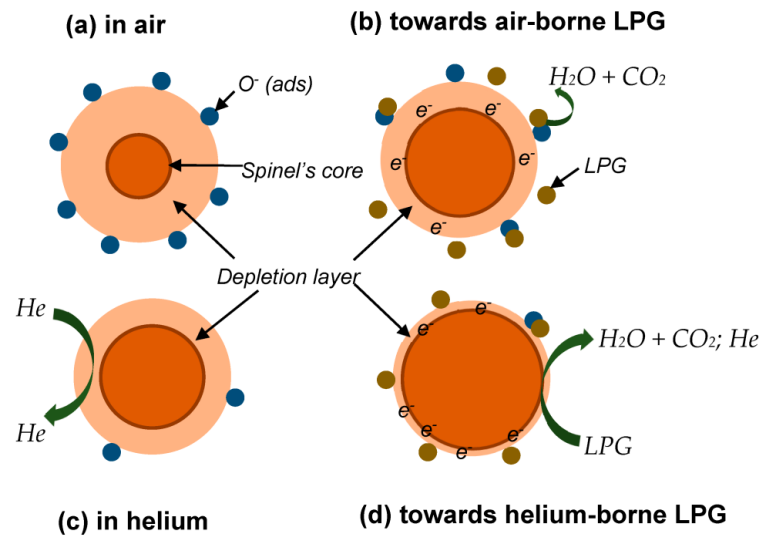
Figure 7. Schematic illustration of the gas sensing mechanism of the $Co_{0.8}Ni_{0.1}Mn_{0.1}Fe_{1.9}Ce_{0.1}O_4$ based sensor (**a**) using air as carrier gas (**b**) toward LPG using dry air as carrier gas, (**c**) using helium as carrier gas (**d**) toward LPG using helium as carrier gas.
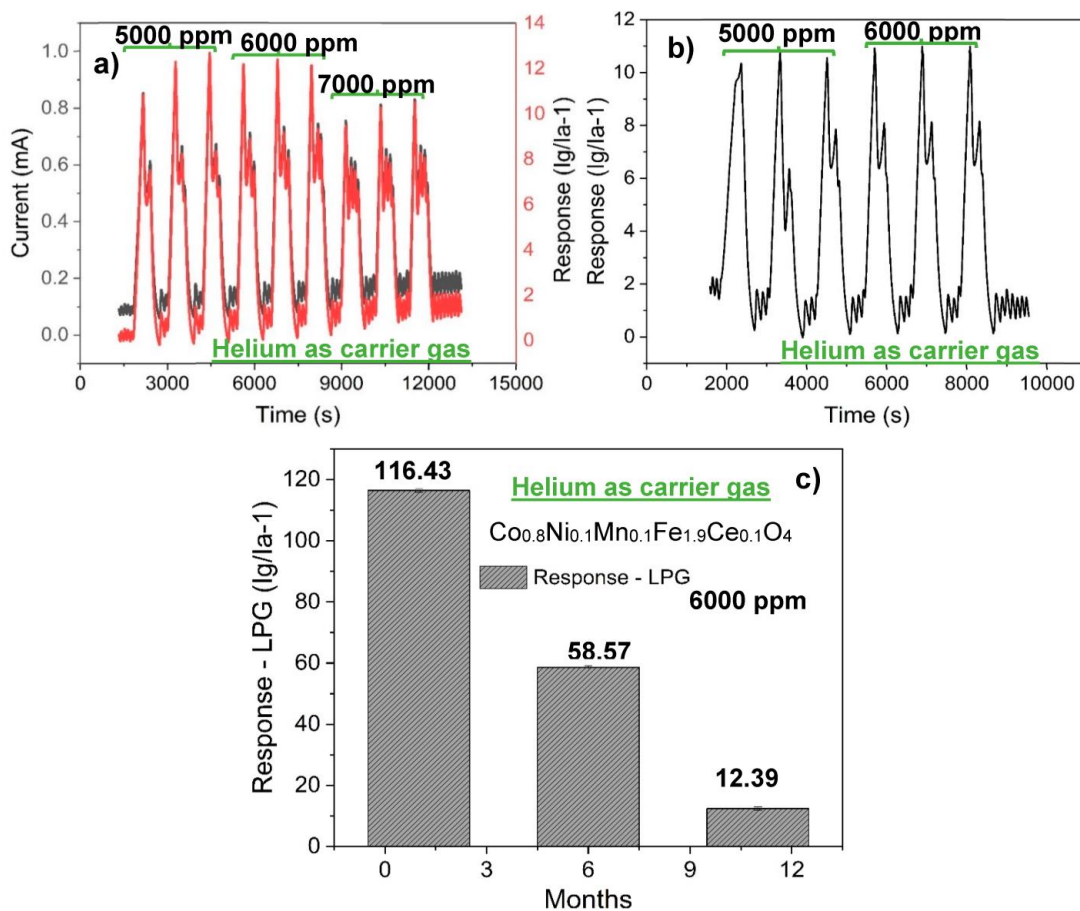
Figure 8. (**a**) Transient current and response curve from the sensitivity of the sensor (S3) toward 5000, 6000 and 7000 ppm of LPG using helium as carrier gas, (**b**) response of S3 toward 5000 and 6000 ppm of LPG using helium as carrier gas in the presence of 50% RH and (**c**) long-term stability of the sensor (S3) using helium as carrier gas.

The long-term stability of the sensor (S3) in helium gas atmosphere is presented in Figure 8c. The sensor retained about 50% of its initial sensitivity toward LPG over 6 months. Surprisingly, in the following 5 months, the response drastically diminished relative to the initial response. This drastic decrease in response could be the effect of the series of current instabilities the sensor underwent while detecting LPG over this period. This instability, otherwise called current oscillation, occurred at the peaks (marked with a red arrow in Figure 6d), as well as at the relaxation (marked with a green arrow in Figure 6d). This could have caused enormous stress for the sensor and thereby rapidly reduced its efficiency.

The result of this work in comparison to other works on LPG detection is summarized in Table 4. The performance of the sensor with helium as the carrier is quite remarkable.

Table 4. Comparison of the performance of the double-substitution spinel with other sensor materials in LPG detection.

Material	Carrier Gas	Operating Temp. (°C)	Concentration (ppm)	Response	Ref.
ZnO	Dry air	200	100	49%	[44]
CdO	Dry air	50	10,000	4.6%	[45]
$MgFe_2O_4$	Dry air	225	10,000	395.47	[30]
$MgFe_2O_4/BiVO_4$	Dry air	50	500	58%	[23]
$Sn-CuFe_2O_4$	Dry air	25	2000	78%	[16]
$Co_{0.8}Ni_{0.1}Mn_{0.1}Fe_{1.9}Ce_{0.1}O_4$	Dry air	225	3000	3.35	This work
$Co_{0.8}Ni_{0.1}Mn_{0.1}Fe_{1.9}Ce_{0.1}O_4$	Helium gas	225	6000	116.43	This work

4. Conclusions

The gas sensing performance of a double-substitution spinel is reported in this work. Both doped and pristine Cobalt ferrite spinels, prepared using the glycol-thermal method, were exposed to flammable gases using dry air, helium gas, nitrogen gas and argon gas as carrier gases at different times. The gas sensing performance of S3, i.e., the sample with the chemical formula $Co_{0.8}Ni_{0.1}Mn_{0.1}Fe_{1.9}Ce_{0.1}O_4$, toward 6000 ppm concentration of LPG using helium as the carrier gas was relatively high. When helium was used as the carrier gas, the sensor experienced a series of current oscillations upon LPG detection, at the peaks as well as at relaxation. In addition, the sensor's response declined from 7000 ppm of LPG concentration, contrary to expectations. The gas sensing performance of the sensor when dry air was used as the carrier gas was low, and its LPG sensing was accompanied by current oscillation, which was observed to have been triggered by fluctuation in the operating temperature. Moreover, the sensors underwent n-type to p-type charge carrier transition from 4000 ppm concentration of LPG. This may be the reason for their poor performance in dry air. Using nitrogen as the carrier gas, the sensitivity pattern of the sensor (S3) was similar to that observed in dry air, as the charge carrier transition of the sensor was also observed. The response of the sensor toward LPG using argon as the carrier gas was poor and unquantifiable. The response of the sensor after a period of 11 months was found to have diminished significantly. However, it exhibited very high resistance toward 50% relative humidity.

Currently, there is no adequate knowledge to explain the phenomena accompanying LPG sensing using dry air and helium as the carrier gases. A more comprehensive study is very crucial for a better understanding of the phenomena and in order to fabricate efficiently operable sensors despite the anomalous phenomena.

References

1. Majhi, S.M.; Naik, G.K.; Lee, H.-J.; Song, H.-G.; Lee, C.-R.; Lee, I.-H.; Yu, Y.-T. Au@NiO core-shell nanoparticles as p-type gas sensor: Novel synthesis, characterization, and their gas sensing properties with sensing mechanism. *Sens. Actuators B* **2018**, *268*, 223–231. [CrossRef]
2. Bhati, V.S.; Kumar, M.; Banerjee, R. Gas sensing performance of 2D nanomaterials/metal oxide nanocomposites: A review. *J. Mater. Chem. C* **2021**, *9*, 8776. [CrossRef]
3. Qin, W.; Yuan, Z.; Gao, H.; Zhang, R.; Meng, F. Perovskite-structured LaCoO3 modified ZnO gas sensor and investigation on its gas sensing mechanism by first principle. *Sens. Actuators B Chem.* **2021**, *341*, 130015. [CrossRef]
4. Ji, H.; Zeng, W.; Li, Y. Gas sensing mechanisms of metal oxide semiconductors: A focus review. *Nanoscale* **2019**, *11*, 22664. [CrossRef]
5. Shah, V.; Bhaliya, J.; Patel, G.M.; Joshi, P. Room-Temperature Chemiresistive Gas Sensing of SnO_2 Nanowires: A Review. *J. Inorg. Organomet. Polym. Mater.* **2022**, *32*, 741–772. [CrossRef]
6. Zhu, L.; Zeng, W. Room-temperature gas sensing of ZnO-based gas sensor: A review. *Sens. Actuators A* **2017**, *267*, 242–261. [CrossRef]
7. Malik, R.; Tomer, V.K.; Mishra, Y.K.; Lin, L. Functional gas sensing nanomaterials: A panoramic view. *Appl. Phys. Rev.* **2020**, *7*, 021301. [CrossRef]
8. Thangamani, G.J.; Khadheer Pasha, S.K. Titanium dioxide (TiO_2) nanoparticles reinforced polyvinyl formal (PVF) nanocomposites as chemiresistive gas sensor for sulphur dioxide (SO_2) monitoring. *Chemosphere* **2021**, *275*, 129960. [CrossRef]
9. Walker, J.M.; Akbar, S.A.; Morris, P.A. Synergistic effects in gas sensing semiconducting oxide nano-heterostructures: A review. *Sens. Actuators B Chem.* **2019**, *286*, 624–640. [CrossRef]
10. Kumar, E.R.; Kanzim, A.S.; Janani, K. Effect of annealing on particle size microstructure and gas sensing properties of Mn substituted $CoFe_2O_4$ nanoparticles. *J. Magn. Magn. Mater.* **2016**, *417*, 122–129. [CrossRef]
11. Zhou, T.; Cao, S.; Zhang, R.; Tu, J.; Fei, T.; Zhang, T. Effect of cation substitution on the gas sensing performances of ternary spinel MCo_2O_4 (M = Mn, Ni, and Zn). *J. Appl. Mater. Interfaces* **2019**, *11*, 28023–28032. [CrossRef] [PubMed]
12. Patil, J.; Nadargi, D.; Mulla, I.S.; Suryavanshi, S.S. Spinel $MgFe_2O_4$ thick films: A colloidal approach for developing gas sensors. *Mater. Lett.* **2018**, *213*, 27–30. [CrossRef]

13. Shozi, N.N.; Kortidis, I.; Mkwae, P.S.; Chonco, N.P.; Leshabane, N.; Jozela, M.; Kroon, R.E.; Swart, H.C.; Nkosi, S.S. Extremely sensitive and selective flammable liquefied hydrocarbon gas sensing and interdependence of fluctuating operating temperature and resistance: Perspective of rare-earth doped cobalt nanoferrites. *J. Alloys Compd.* **2021**, *859*, 157846. [CrossRef]

14. Koli, P.B.; Kapadnis, K.H.; Deshpandhe, U.G. Nanocrystalline-modified nickel ferrite films: An effective sensor for industrial and environmental gas pollutant detection. *J. Nanostructure Chem.* **2019**, *9*, 95–110. [CrossRef]

15. Nemufulwi, M.I.; Swart, H.C.; Mhlongo, G.H. A comprehensive comparison study on magnetic behaviour, defects-related emission and Ni substitution to clarify the origin of enhanced acetone detection capabilities. *Sens. Actuators B. Chem.* **2021**, *339*, 129860. [CrossRef]

16. Manikandan, V.; Singh, M.; Yadav, B.C.; Mane, R.S.; Vigneselvand, S.; Mirzaei, A. Chandrasekaran. Room temperature LPG sensing properties of tin substituted copper ferrite (Sn-CuFe$_2$O$_4$) thin film. *Mater. Chem. Phys.* **2020**, *240*, 122265. [CrossRef]

17. Wu, S.; Li, X.; Xu, Y.; Wu, J.; Wang, Z.; Han, Y.; Zhang, X. Hierarchical spinel Ni$_x$Co$_{1-x}$Fe$_2$O$_4$ microcubes derived from Fe-based MOF for high-sensitive acetone sensor. *Ceram. Int.* **2018**, *44*, 19390–19396. [CrossRef]

18. Gonçalves, J.M.; Rocha, D.P.; Silva, M.N.T.; Martins, P.R.; Nossol, E.; Angnes, L.; Rout, C.S.; Munoz, R.A.A. Feasible strategies to promote the sensing performances of spinel MCo$_2$O$_4$ (M = Ni, Fe, Mn, Cu and Zn) based electrochemical sensors: A review. *J. Mater. Chem. C* **2021**, *9*, 7852–7887. [CrossRef]

19. Almessiere, M.A.; Slimani, Y.; Baykal, A. Synthesis and characterization of Co$_{1-2x}$Ni$_x$Mn$_x$Fe$_{2-y}$Ce$_y$O4 nanoparticles. *J. Rare Earths* **2020**, *38*, 188–194. [CrossRef]

20. Shankar, P.; Rayappan, J.B.B. Gas sensing mechanism of metal oxide: The role of ambient atmosphere, type of semiconductor and gases—A review. *Sci. Lett. J.* **2015**, *4*, 126.

21. Zhang, J.; Qin, Z.; Zeng, D.; Xie, C. Metal-oxide-based semiconductor gas sensor: Screening, preparation and integration. *J. Phys. Chem.* **2017**, *19*, 6313–6329. [CrossRef]

22. Pi, W.; Chen, X.; Humayun, M.; Yuan, Y.; Dong, W.; Zhang, G.; Chen, B.; Fu, Q.; Lu, Z.; Li, H.; et al. Highly Sensitive Chemiresistive H$_2$S Detection at Subzero Temperature over the Sb-Doped SnO$_2$@gC$_3$N$_4$ Heterojunctions under UV Illumination. *Appl. Mater. Interfaces* **2023**, *11*, 14979–14989.

23. Munindra, P.; Reddy, M.S.B.; Rani, B.G.; Jayarambabu, N.; Kailasa, S.; Rao, P.S.S.; Rao, K.V. A high-performance low-temperature LPG detection by MgFe$_2$O$_4$/BiVO$_4$ chemiresistive sensor. *J. Mater. Sci. Mater. Electron.* **2020**, *31*, 2370–2377. [CrossRef]

24. Almessiere, M.A.; Slimani, Y.; Ali, S.; Baykal, A.; Ercan, I.; Sozeri, H. Nd^{3+} Ion-Substituted Co$_{1-2x}$Ni$_x$Mn$_x$Fe$_{2-y}$Nd$_y$O$_4$ Nanoparticles: Structural, Morphological, and Magnetic Investigations. *J. Inorg. Organomet. Polym. Mater.* **2019**, *29*, 783–791. [CrossRef]

25. Almessiere, M.A.; Slimani, Y.; Güner, S.; Nawaz, M.; Baykal, A.; Aldakheel, F.; Akhtar, S.; Ercan, I.; Beleli, I.; Ozçelik, B. Magnetic and structural characterization of Nb^{3+}-substututed CoFe$_2$O$_4$ nanoparticles. *Ceram. Int.* **2019**, *45*, 8222–8232. [CrossRef]

26. Rani, B.J.; Ravina, M.; Saravanakumar, B.; Ravi, G.; Ganesh, V.; Ravichandran, S.; Yuvakkumar, R. Ferrimagnetism in cobalt ferrite (CoFe$_2$O$_4$) nanoparticles. *Nanostructures Nano-Objects* **2018**, *14*, 84–91. [CrossRef]

27. Motaung, D.E.; Tshabalala, Z.P.; Makgwane, P.R.; Mahmoud, F.A.; Oosthuizeni, D.N.; Cummings, F.R.; Leshabane, N.; Hintsho-Mbita, N.; Li, X.; Ray, S.S.; et al. Multi-Functioning of CeO$_2$-SnO$_2$ Heterostructure as Room Temperature Ferromagnetism and Chemiresistive Sensors. *J. Alloys Compd.* **2021**, *906*, 164317. [CrossRef]

28. Mayank, V.S.K.N.; Sumathi, S. Photocatalytic performance of cerium doped copper aluminate nanoparticles under visible light irradiation. *J. Taiwan Inst. Chem. Eng.* **2019**, *95*, 602–615.

29. Nurhasanah, I.; Safitri, W.; Arifin, Z.; Subagio, A.; Windarti, T. Antioxidant activities and dose enhancement factor of CeO$_2$ nanoparticles synthesized by precipitation method. *IOP Conf. Ser. Mater. Sci. Eng.* **2018**, *432*, 012031. [CrossRef]

30. Mkwae, P.S.; Ogundipe, S.A.; Jozela, M.; Revaprasadu, N.; Nkosi, S.S. The heat rate kinetics on the liquefied hydrocarbon gases sensing and food quality control detecting strategy. *Mater. Chem. Phys.* **2022**, *277*, 125550. [CrossRef]

31. Chandamma, N.; Kumar, M.S.; Shankarmurthy, G.J.; Melagiriyappa, E.; Nagaraja, K.K. Effect of gamma irradiation on some electrical and dielectric properties of Ce^{3+} substituted Ni-Zn nano ferrites. *Chin. J. Phys.* **2017**, *55*, 1729–1738. [CrossRef]

32. Wang, J.; Sun, A.; Jiang, Y.; Huang, X.; Shao, L.; Zhang, Y. Structural and magnetic properties of Ce^{3+} doped Mg-Co ferrite prepared by sol–gel method. *J. Mater. Sci. Mater. Electron.* **2022**, *33*, 11881–11895. [CrossRef]

33. Li, L.-Z.; Zhong, X.-X.; Wang, R.; Tu, X.Q.; He, L.; Wang, F.-H. Effects of Ce substitution on structural and electromagnetic properties of NiZn nano ferrite. *J. Magn. Magn. Mater.* **2019**, *475*, 1–4. [CrossRef]

34. Mustapha, S.; Tijani, J.O.; Ndamitso, M.M.; Abbdulkareem, A.S.; Shuahib, D.T.; Amigun, A.T.; Abubakar, H.L. Facile synthesis and characterisation of TiO$_2$ nanoparticles: X-ray peak profile analysis using Williamson-Hall and Debye-Scherrer methods. *Int. Nano Lett.* **2021**, *11*, 241–261. [CrossRef]

35. Khalfaoui, M.; Knani, S.; Hachicha, M.A. Ben Lamine. New theoretical expreesions for the five adsorption isotherms classifield by BET based on statistical physics treatment. *J. Colloid Interface Sci.* **2003**, *263*, 350–356. [CrossRef] [PubMed]

36. Hailstone, R.K.; DiFrancesco, A.G.; Leong, J.G.; Allston, T.D.; Reed, K.J. A study of lattice expansion in CeO$_2$ nanoparticles by transmission electron microscopy. *J. Phys. Chem. C* **2009**, *113*, 15155–15159. [CrossRef]

37. de Lima Alves, T.M.; Amorim, B.F.; Torres, M.A.M.; Bezerra, C.G.; de Medeiros, S.N.; Gastelois, P.L.; Outon, L.E.F.; de Almeida Macedo, W.A. Wasp-waisted behavior in magnetic hysteresis curves of CoFe$_2$O$_4$ Nano powder at a low temperature: Experimental evidence and theoretical approach. *J. R. Soc. Chem. Adv.* **2017**, *7*, 22187.

38. Gumbi, S.W.; Mkwae, P.S.; Kortidis, I.; Kroon, R.E.; Swart, H.C.; Moyo, T.; Nkosi, S.S. Electronic and simple oscillatory conduction in ferrite gas sensing: Gas-sensing mechanism, Long-term gas monitoring, Heat transfer, and other anomalies. *J. Appl. Mater. Interfaces* **2020**, *12*, 43231–43249. [CrossRef] [PubMed]

39. Mirzaei, A.; Bonyani, M.; Torkian, S.; Feizpour, M.; Bonavita, A.; Leonardi, S.G.; Neri, G. A comparative study on the electrical and gas sensing properties of thick films prepared with synthesized nano-sized and commercial micro-sized Fe_2O_3 powders. *Process. Appl. Ceram.* **2017**, *11*, 265–274. [CrossRef]

40. Rai, P.; Majhi, S.M.; Yu, Y.-T.; Lee, J.-H. Nobel metal@metal oxide semiconductor core@shell nano-architectures as a new platform for gas sensing applications. *RSC Adv.* **2015**, *5*, 76229. [CrossRef]

41. Nikolic, M.V.; Milovanovic, V.; Vasiljevic, Z.Z.; Stamenkovic, Z. Semiconductor gas sensors: Materials, technology, design, and application. *Sensors* **2020**, *20*, 6694. [CrossRef] [PubMed]

42. Das, S.; Mojumder, S.; Saha, D.; Pa, M. Influence of major parameters on the sensing mechanism of semiconductor metal oxide based chemiresitive gas sensors: A review focused on personalized healthcare. *Sens. Actuators B. Chem.* **2022**, *352*, 131066. [CrossRef]

43. Staerz, A.; Weimar, U.; Barsan, N. Current state of knowledge on the metal oxide-based gas sensing mechanism. *Sens. Actuators B. Chem.* **2022**, *358*, 131531. [CrossRef]

44. Choudhary, S.; Annapoorni, S.; Malik, R. Evolution and growth mechanism of hexagonal ZnO nanorods and their LPG sensing response at low operating temperature. *Sens. Actuactors A Phys.* **2019**, *293*, 207–214. [CrossRef]

45. Nakate, U.T.; Patil, P.; Ghule, B.; Nakate, Y.T.; Ekar, S.; Ambare, R.C.; Mane, R.S. Room temperature LPG sensing properties using spray pyrolysis deposited nano-crystalline CdO thin films. *Surf. Interfaces* **2019**, *17*, 100339. [CrossRef]